Discover Oncology

ANALYSIS Open Access

Exploring tumor heterogeneity and drug resistance in cervical cancer through single-cell and bulk transcriptomics

Yinxia Yang[1], Sirong Cheng[1], Yuxuan Zhong[1], Pengyu Sun[1], Xiaoru Deng[1] and Bohui Zhou[1,2*]

*Correspondence:
Bohui Zhou
zhoubohui@sxbqeh.com.cn
[1]Shanxi Bethune Hospital, Shanxi Academy of Medical Sciences, Third Hospital of Shanxi Medical University, Tongji Shanxi Hospital, Taiyuan 030032, China
[2]Department of Obstetrics and Gynecology, Shanxi Bethune Hospital, Shanxi Academy of Medical Sciences, Third Hospital of Shanxi Medical University, Tongji Shanxi Hospital, Taiyuan 030032, China

Abstract

Background Cervical cancer, as one of the most common types of malignant tumors in women, poses a significant threat to the health and survival of women worldwide. Tumor drug resistance has emerged as a critical bottleneck severely limiting the efficacy of current cervical cancer treatment strategies, making it imperative to delve deeper into the underlying mechanisms for improved therapeutic outcomes.

Methods Spatial transcriptomics and single-cell sequencing technologies were employed. Single-cell sequencing was used to uncover the heterogeneity in cervical cancer development. Pseudotime analysis, exploration of cell communication pathways, and spatial transcriptomics were further applied to investigate the roles of relevant molecules.

Results This study reveals an abundance of PI3 + neoplastic (NEO) in tumors and SLC40A1 + NEO cells in HSIL samples. These cell populations may play crucial roles in the development of drug resistance, as they could potentially alter the tumor microenvironment and interfere with the efficacy of therapeutic agents. Pseudotime analysis, cell communication pathways, and spatial transcriptomics highlight the pivotal role of LGALS9 and its ligands, offering new insights for early diagnosis, molecular typing, prognosis evaluation, and personalized treatment of cervical cancer.

Conclusion Our findings reveal that high expression of LGALS9 suppresses T cell function, fosters a strongly immunosuppressive tumor microenvironment, and is associated with chemotherapy resistance, ineffective immunotherapy, and poor prognosis. LGALS9 may serve as a biomarker for predicting immunotherapy response. This knowledge has the potential to facilitate early diagnosis, precise molecular typing, accurate prognosis evaluation, and the development of personalized treatment strategies that can overcome tumor drug resistance and improve patient outcomes.

Keywords Human papillomavirus, Cervical cancer, Molecular typing, Spatial transcriptomics, Heterogeneity, Drug resistance

1 Introduction

Cervical cancer, as one of the most common types of malignant tumors in women, poses a significant threat to the health and survival of women worldwide [1]. According to data from the Global Cancer Observatory (GLOBOCAN) developed by the International Agency for Research on Cancer (IARC) in 2020, there were approximately 604,000 new cases of cervical cancer and about 342,000 deaths globally, with both incidence and mortality rates ranking fourth worldwide [2]. The high incidence and mortality rates of cervical cancer not only have a major impact on society but also impose profound psychological stress on patients and their family members, as well as a substantial economic burden on the economy. Hence, cervical cancer has become one of the primary public health concerns attracting the attention of the public and researchers alike [3].

Cervical cancer is unequivocally caused, with the vast majority (approximately 95%) of cases being attributable to persistent infection by high-risk human papillomavirus (hrHPV) [4]. Among the histological subtypes of cervical cancer, squamous cell carcinoma (SCC) is the most prevalent, accounting for about 70%, whereas adenocarcinoma (ADC) comprises approximately 20% to 25% [5]. Cervical squamous intraepithelial lesions (SIL), a group of conditions closely associated with invasive cervical cancer, are predominantly observed in women aged 25 to 35 years. While most low-grade squamous intraepithelial lesions (LSIL) may regress naturally, high-grade squamous intraepithelial lesions (HSIL) possess the potential to transform into cancer [6]. The identification of HSIL reflects the continuum in the progression of cervical cancer, making the screening for SIL and timely treatment of high-grade lesions an effective measure for preventing invasive cervical cancer. Advances in genomics have gradually uncovered that within the same type of HPV, there exists a variety of variant lineages and sublineages, which significantly differ in their carcinogenic potential [7, 8]. Single-cell sequencing technology, by analyzing gene expression at the single-cell level, enables researchers to identify and characterize different cellular populations within tumors, including tumor cells, immune cells, and fibroblasts, thereby revealing their molecular characteristics and functional states. This high-resolution perspective provides an unprecedented opportunity for a deeper understanding of tumor heterogeneity [9, 10]. Spatial transcriptomics, by integrating gene expression data with information on the spatial distribution of cells, allows researchers to explore the precise location of cells within tumor tissue and their surrounding microenvironment, offering a new dimension to understand how cells interact spatially and influence tumor progression. This study integrates spatial transcriptomics, single-cell sequencing, and public cervical squamous cell carcinoma (CESC) survival data to thoroughly explore cervical cancer tumor heterogeneity and its role in tumor progression and immune evasion. It identifies an abundance of PI3 + neoplastic (NEO) in tumors and SLC40A1 + NEO cells in HSIL samples. Pseudotime analysis reveals multiple pathways for tumor cells, with terminal branches rich in PI3 + NEO samples. Lower levels of CXCL13 + NKT cells are closely linked to prognosis. Cell communication analysis highlights the upregulation of MK and GALECTIN pathways in tumor tissues, emphasizing the critical role of the LGALS9_CD44 ligand-receptor pair. This comprehensive molecular and spatial analysis aims to provide new theoretical and experimental insights for early diagnosis, molecular typing, prognosis assessment, and personalized treatment of cervical cancer.

2 Methods

2.1 Acquisition and processing of transcriptome data

In the course of investigating the molecular mechanisms of cervical cancer and identifying potential biomarkers, analyzing tumor samples' RNA expression profiles and their association with clinical features is crucial. To this end, within the R software environment (version 4.1.3), we utilized the TCGAbiolinks package [11], to download RNA sequencing data and corresponding clinical information for Cervical Squamous Cell Carcinoma and Endocervical Adenocarcinoma from the TCGA database. By querying the TCGA repository, we obtained a cohort comprising RNA-seq data and clinical details of patients with cervical cancer, including survival times and statuses. All RNA sequencing data were provided in Transcripts Per Million (TPM) format, facilitating cross-sample comparisons. To meet the requirements for subsequent analyses, all RNA expression data were converted from TPM format to log2(TPM + 1) format. This transformation aims to improve the normal distribution characteristics of the data and mitigate the impact of extreme values, thereby enhancing the interpretability and robustness of the data.

2.2 Acquisition and processing of single-cell transcriptome sequencing and spatial transcriptome sequencing data

The single-cell dataset was sourced from the GEO database, under the accession GSE208653, comprising three tumor samples positive for HPV, two HSIL samples positive for HPV, and an additional tumor sample from GSE168652, totaling six samples. Analysis was conducted using Seurat package [12]. Cell quality control criteria included mitochondrial content less than 20%, with restrictions for cell UMI counts and gene counts set between 200 and 50,000 and 200–9000, respectively. Data normalization, selection of highly variable genes (2000 genes), and data transformation (mitigating cell cycle effects with parameters vars.to.regress = c ("S.Score", "G2M.Score")) were executed using the functions NormalizeData, FindVariableFeatures, and ScaleData from the Seurat package, respectively. Batch effects were addressed using the harmony method [13].

In further investigations, this study employed advanced dimensionality reduction techniques including UMAP and t-SNE, as well as the Louvain clustering algorithm for delineating cell populations, all of which were selected from the Seurat package. To elucidate the significant gene expression differences between distinct cell populations or cell types, the FindAllMarkers function was utilized, with parameters set to a p-value less than 0.05, a log2 fold change (log2FC) greater than 0.25, and a requirement that the gene's expression proportion in cells exceed 0.1. Additionally, spatial transcriptomics data were derived from the NCBI database project PRJNA860567, encompassing two primary tumor samples and one HSIL sample. Another cervical cancer sample was collected from the 10X Genomics website (https://www.10xgenomics.com/datasets/human-cervical-cancer-1-standard). Using data quality-controlled by the SpaceRanger software [12], the SCTtransform algorithm was applied for data normalization [14], selection of highly variable genes, and data transformation, with an average of 1678 spots, and mean UMI count, gene count, and mitochondrial content of 11138.1, 3466.3, and 6%, respectively. All analyses and visualizations were performed using the Seurat software. In this study, the Conditional Autoregression-based Deconvolution (CARD) algorithm was

employed [15], utilizing single-cell annotation data to accurately predict the cell type of each micro-area (spot) within spatial transcriptomics data. The distribution of cell types in spatial transcriptomics data was extensively visualized using the CARD software. Furthermore, the study utilized the GSVA package and the AddModelScore function of the Seurat package to calculate the score values of various biomarker expression signatures [16], aiming to enhance the understanding of the functional states of cells (Fig. 1).

2.3 Cell annotation and analysis

Initially, this study utilized specific cellular markers for categorizing and identifying cells within the dataset, including: epithelial cell markers EPCAM, KRT18, KRT19, and CDH1; fibroblast markers DCN, THY1, COL1A1, and COL1A2; endothelial cell markers PECAM1, CLDN5, FLT1, and RAMP2; T cell markers CD3D, CD3E, CD3G, and TRAC; NK cell markers NKG7, GNLY, NCAM1, and KLRD1; B cell markers CD79A, IGHM, IGHG3, and IGHA2; mast cell markers KIT, MS4A2, and GATA2. Leveraging these markers, separate isolation and cluster analyses were conducted on epithelial cells, immune cells, and fibroblasts to further explore their roles in tumor heterogeneity. Moreover, analysis outcomes were visually presented through the creation of UMAP, t-SNE, bar graphs, and heatmaps.

2.4 Subclass analysis of each cell group

In this study, employing the standardized analysis protocol provided by the Seurat package, immune cells, epithelial cells, and fibroblasts were individually isolated and purified. Subsequently, based on the identification of specific markers, further subdivision into respective subpopulations was achieved. These specific markers served as the criteria for distinguishing different cellular subgroups. Utilizing Uniform Manifold Approximation and Projection (UMAP) techniques, the distribution characteristics of these subpopulations were visualized, revealing their spatial distribution and interrelations within the samples.

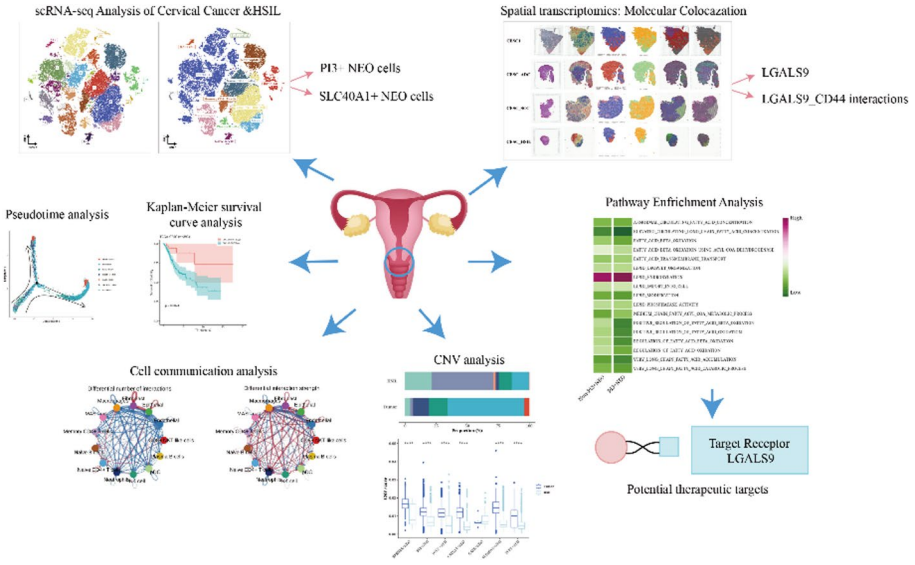

Fig. 1 The flow chart of this study. Single-cell RNA Sequencing, scRNA-seq; Neoplastic, NEO; High-grade Squamous Intraepithelial Lesion, HSIL; Copy Number Variations, CNV

2.5 CNV analysis of single cells

For precise identification of malignant cells within tumor cell subpopulations at the single-cell level, this study employed the InferCNV software tool. This tool, using normal epithelial cells as a reference, conducted copy number variation (CNV) analysis on tumor cell subpopulations. The application of this method aims to delve into the genetic heterogeneity of tumor cells, particularly identifying malignant cells with significant copy number variations. This provides crucial molecular biological evidence for understanding the mechanisms of tumor development and potential therapeutic targets.

2.6 Pseudotime analysis of single cell sequencing

In the field of single-cell research, pseudotime analysis is a pivotal analytical approach for inferring the temporal sequence during cell differentiation or development. In this study, we employed monocle2 software for pseudotime analysis of epithelial cell subpopulations, aiming to elucidate the dynamics of cell differentiation [17]. For this analysis, the DDRTree algorithm was utilized for dimension reduction to optimize data structure, while default parameters were maintained to ensure standardization and reproducibility of the analytical process. Through this approach, we successfully constructed cell differentiation trajectories, providing significant insights into the behavior of epithelial cells under physiological and pathological conditions.

2.7 Transcription factor analysis

In this study, to elucidate the activity of transcription factors and their regulatory networks within various cell subpopulations, we employed the SCENIC software for transcription factor analysis. Specifically, SCENIC analysis was conducted utilizing the motif databases provided by RcisTarget and GRNBoost, following the default parameter settings. The RcisTarget package enabled us to identify significantly overexpressed transcription factor binding motifs within a designated gene list. Furthermore, the AUCell package was utilized to score the activity of each regulon within every cell type, allowing for the accurate assessment of their regulatory functions within the cellular context.

2.8 Cell to cell communication analysis

In this study, the CellChat package was employed to investigate intercellular communication mechanisms [18]. Initially, a CellChat object was constructed by importing the normalized gene expression matrix using the CellChat function. Subsequently, a series of preprocessing steps were undertaken using the identifyCESCerExpressedGenes, identifyCESCerExpressedInteraction, and ProjectData functions, all set to their default parameters. Further, a range of potential ligand-receptor interactions were successfully identified through the application of the computeCommunProb, filterCommunication, and computeCommunProbPathway functions. Ultimately, an exhaustive cell communication network was generated using the aggregateNet function, offering significant insights into the intricate interactions between cells.

2.9 Statistic analysis

All data processing, statistical analysis, and graph plotting were conducted in R software, version 4.1.3. The Pearson correlation coefficient was utilized to assess the correlation between two continuous variables. Differences between categorical variables were

compared using the chi-square test, while differences between continuous variables were evaluated using the Wilcoxon rank-sum test or the t-test. The survminer package was employed to determine the optimal cutoff values in survival analysis. Cox regression analysis and Kaplan-Meier survival curve analysis were performed using the survival package.

3 Result

3.1 Single cell expression map of CESC

After performing dimensionality reduction and clustering analysis on single-cell data, our study successfully identified 30 cell clusters (Fig. 2A). Utilizing specific cell markers, such as epithelial cell markers ("EPCAM", "KRT18", "KRT19", "CDH1"), fibroblast markers ("DCN", "THY1", "COL1A1", "COL1A2"), endothelial cell markers ("PECAM1", "CLDN5", "FLT1", "RAMP2"), T cell markers ("CD3D", "CD3E", "CD3G", "TRAC"), NK cell markers ("NKG7", "GNLY", "NCAM1", "KLRD1"), B cell markers ("CD79A", "IGHM",

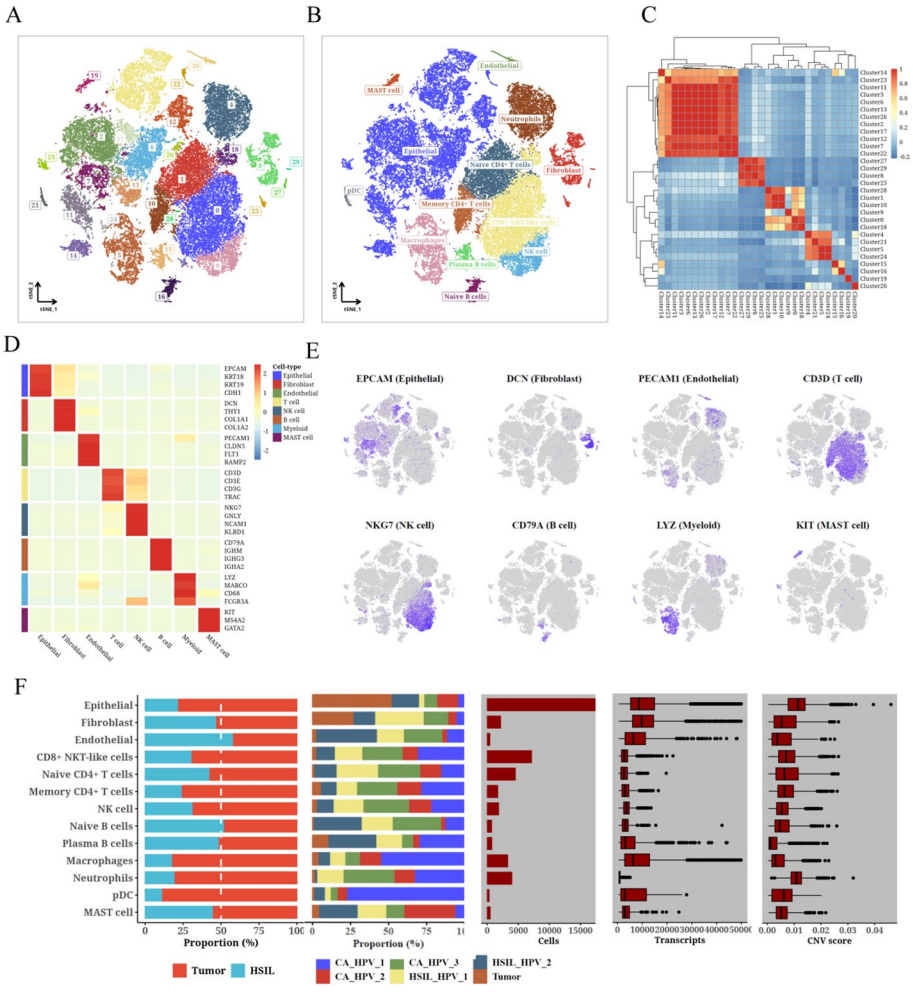

Fig. 2 Single cell classification results of CESC, A-B. t-SNE plots colored by clustering and cell types; C. Correlation matrix based on marker gene expression across clusters; D. Heatmap of marker gene expression across cell types; E. t-SNE plots illustrating marker gene expression profiles; F. A composite chart detailing the cellular source, patient composition, cell numbers, transcript detection, and CNV status across different cell types. t-Distributed Stochastic Neighbor Embedding, t-SNE; Cancer, CA; High-grade Squamous Intraepithelial Lesion, HSIL; Human Papillomavirus, HPV; Copy Number Variations, CNV

"IGHG3", "IGHA2"), and mast cell markers ("KIT", "MS4A2", "GATA2"), we plotted the expression bubble charts of marker genes for each cluster group. Based on the expression characteristics of these marker genes, clusters were annotated as corresponding cell types (Fig. 2B). Furthermore, by applying the expression matrix of marker genes for Pearson correlation analysis and constructing a correlation heatmap (Fig. 2C), we revealed a high consistency between clustering results and cell type classification. Additionally, our study also presented the expression heatmaps (Fig. 2D) and t-SNE plots (Fig. 2E) of marker genes for each cell type, thereby verifying the accuracy of cell type identification. With the aid of Sc-Type software, a further subclassification of immune cells was conducted, and a comparative analysis of cell source composition, patient composition, cell numbers, transcript detection numbers, and CNV was performed for different cell types (Fig. 2F).

3.2 Spatial transcriptome data analysis at CESC

In this study, we meticulously analyzed four spatial transcriptomics samples. By employing the inferCNV software, in conjunction with the CARD algorithm and deconvolution techniques, we assessed the CNV status of each spatial spot and analyzed the cellular composition of each spot in the spatial transcriptomics data, utilizing cell type information from existing single-cell data. Spots annotated with tumor cells were categorized as tumor cells, whereas other cells were considered non-tumor cells. For the selected samples, we individually presented their H&E staining images, CNV score distributions, cellular composition, differentiation between tumor and non-tumor cells, and clustering results of tumor and non-tumor cells (Fig. 3A). The observations revealed that the samples CESC1, CESC_SCC, and CESC_HSIL had a higher proportion of tumor/epithelial overall cellular composition, while the CESC_ADC sample exhibited a relatively lower proportion of tumor/epithelial overall cellular composition, predominantly consisting of fibroblasts (Fig. 3A). Subsequently, spots annotated as tumor or non-tumor cells underwent separate dimension reduction and clustering analyses, where tumor cells were divided into four subgroups, and non-tumor cells into five subgroups (Fig. 3B-E). Through tSNE plots, we illustrated the composition, CNV status, and patient makeup of these subgroups, and computed and depicted the expression heatmaps of marker genes for each subgroup. The cellular type of distribution in the CESC1 sample showed a significant enrichment of fibroblasts, tumor cells, B cells, and myeloid cells (Fig. 3F). Moreover, we explored the cellular composition differences between Tumor and HSIL samples, finding that HSIL samples were predominantly composed of epithelial cells, whereas Tumor samples were rich in non-tumor cells, such as fibroblasts (Fig. 3G).

3.3 Subclassification of tumor cells

Through meticulous single-cell data analysis, this study has achieved precise isolation of tumor cells and conducted specialized dimensional reduction and clustering analysis on them. This process identified seven distinct tumor/epithelial cell subgroups (Fig. 4A). Bar graphs allowed us to observe the differences in cell composition from various samples, with Tumor samples significantly enriched with PI3 + NEO cells, while HSIL samples predominantly contained SLC40A1 + NEO cells. Differential gene expression analysis of these subgroups further revealed the specificity of differentially expressed genes among each subgroup (Fig. 4B). Moreover, through enrichment analysis of these

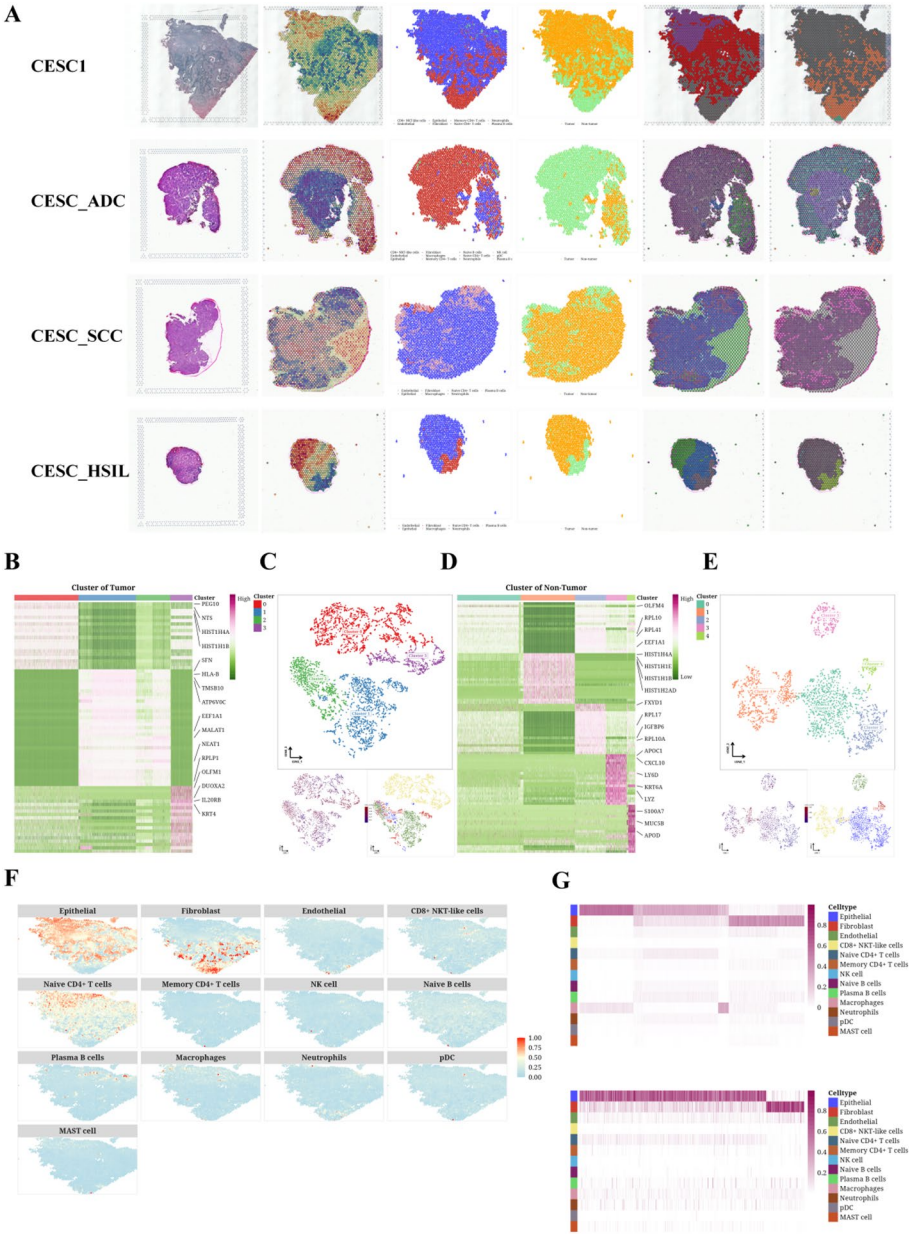

Fig. 3 Results of spatial transcriptome data analysis by Cervical Squamous Cell Carcinoma and Endocervical Adenocarcinoma (CESC), (A) H&E staining images, Copy Number Variations (CNV) score distributions, cell type compositions, tumor versus non-tumor mappings, and clustering results for both tumor and non-tumor cells; (B) The heatmap shows the expression levels of marker genes across tumor cell subgroups; C-E. t-Distributed Stochastic Neighbor Embedding (t-SNE) plots detailing tumor cell subgroup compositions, CNV conditions, and patient compositions, along with equivalent analyses for non-tumor cells; F-G. Cell type distribution for patient CESC1 across various spots is visualized, and differences in cell composition between tumor and High-grade Squamous Intraepithelial Lesion (HSIL) samples are examined through heatmaps, providing insights into the cellular and molecular landscape of cervical cancer

marker genes in Gene Ontology Biological Processes (GOBP), we mapped their respective related biological functions.

Further analysis compared the CNV conditions of different cell types from various sample sources, revealing significant differences, especially CNVs in tumor samples were significantly higher than those in HSIL samples (Fig. 4C). Concurrently, this study also

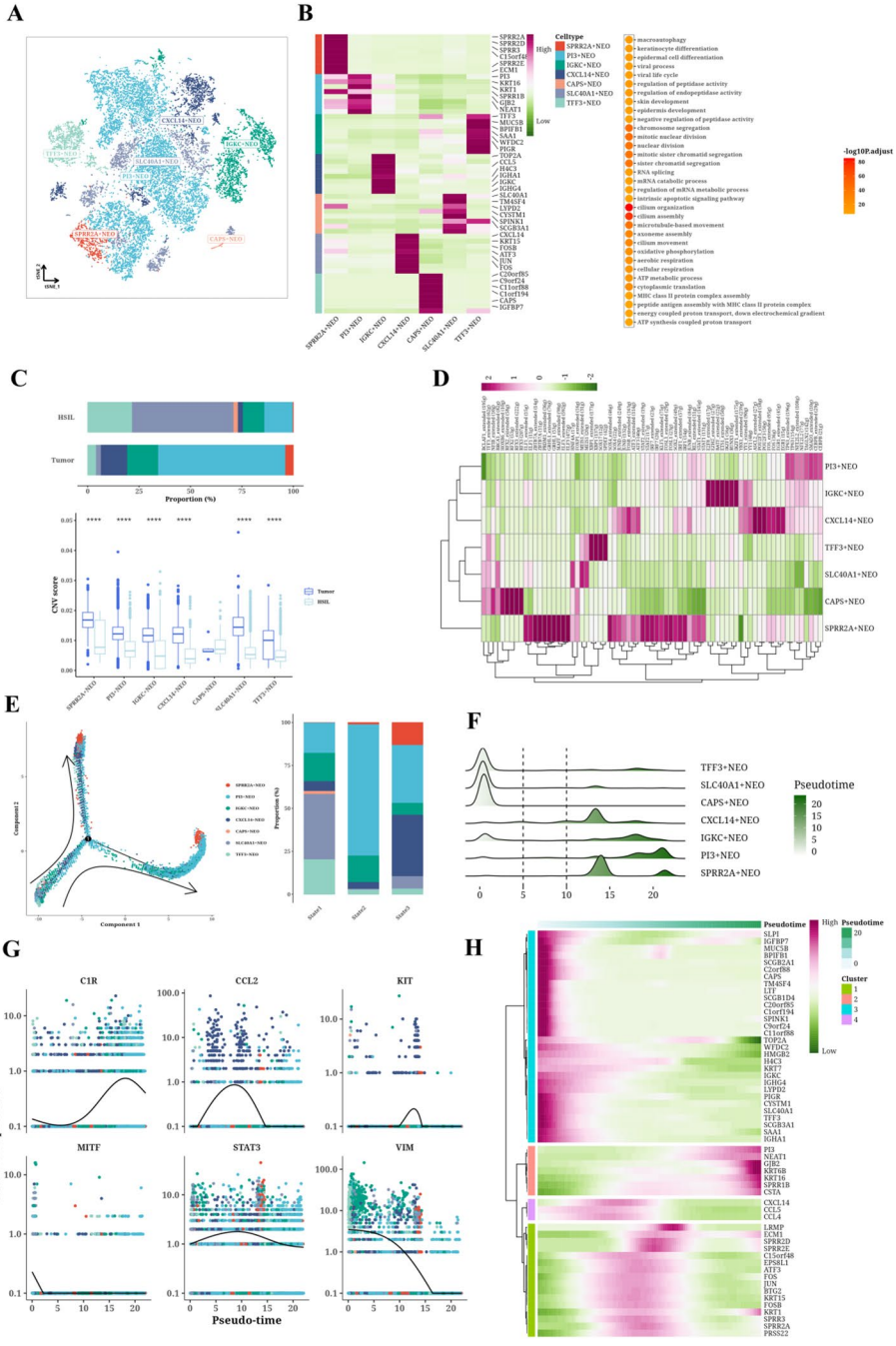

Fig. 4 Results of a tumor cell sub-classification analysis, (A) t-Distributed Stochastic Neighbor Embedding (tSNE) plots colored by cluster classification; (B) Expression heatmaps and corresponding gene ontology (GO) enrichment analysis; (C) Copy Number Variations (CNV) box plots for each cell type and origin; (D) Transcription factor enrichment heatmaps; (E) Cell trajectory analysis with a composition bar chart for each state branch; (F) Pseudotime ridge plots and gene expression heatmaps; G-H. Pseudotime scatter plots for six genes

analyzed the transcription factors of each cell type, and the heatmaps displayed their enrichment for different transcription factors (Fig. 4D).

The execution of cell trajectory analysis marked another significant advancement of this study. Selecting cells from HSIL samples as the starting point, the analysis revealed multiple paths to different endpoints, suggesting the potential existence of different subtypes of cervical cancer, with each endpoint branch containing many PI3 + NEO

samples (Fig. 4E). Pseudotime analysis found that TFF3 + NEO, SLC40A1 + NEO, and CAPS + NEO cells were primarily at the early stages of development, while CXCL14 + NEO and SPRR2A + NEO cells were in an intermediate state, with most other cell types at the end of the process (Fig. 4F). Finally, pseudotime scatter plots were analyzed for six key genes (MITF, KIT, VIM, CCL2, C1R, STAT3) (Fig. 4G-H).

3.4 Functional analysis of PI3 + NEO cells

Our investigation revealed significant differences in the proportion of PI3 + NEO cells between tumor samples and HSIL samples, with tumor samples containing a higher abundance of PI3 + NEO cells (Fig. 5A). We identified differentially expressed genes between PI3 + NEO cells and non-PI3 + NEO cells, visualized in an expression heatmap (Fig. 5B). Lipid metabolism pathways from the MSigDB database were selected to calculate signature scores for both cell groups, illustrated in a heatmap to highlight their differences (Fig. 5C). A notable variance in FATTY_ACID_BETA_OXIDATION between the groups was observed, alongside a significant enrichment of the transcription factor SMAD4 in PI3 + NEO cells, as shown by its expression in spatial transcriptomics data (Fig. 5D). The distribution of FATTY_ACID_BETA_OXIDATION scores among patients with CESC1, CESC_ADC, and CESC_SCC, with cells categorized by the average expression of SMAD4, revealed a violin plot indicating significant differences between the two cell groups (Fig. 5E).

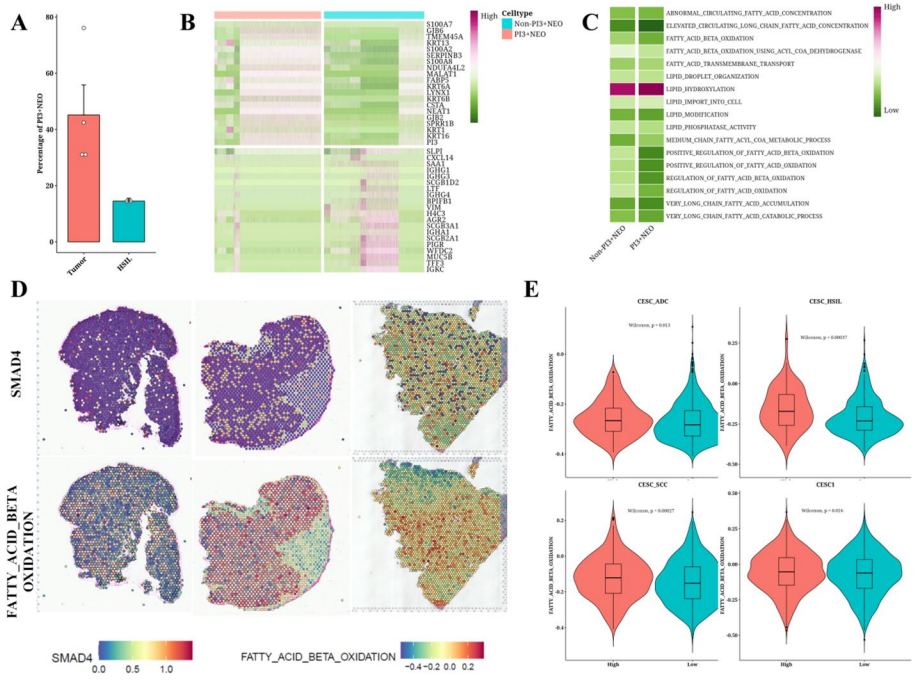

Fig. 5 Functional analysis of PI3 + Neoplastic (NEO) cells, (A) Histogram of the proportion of PI3 + NEO cells in each sample source; (B) Heatmap of differential gene expression in PI3 + NEO cells and non-PI3 + NEO cells; (C) Heatmap of signature Scores of lipid metabolity-related pathways in PI3 + NEO cells and non-PI3 + NEO cells; (D) Expression space diagram of transcription factor SMAD4 and FATTY_ACID_BETA_OXIDATION scores in idled data of CESC1, CESC_ADC, and CESC_SCC patients; (E) Differences in ATTY_ACID_BETA_OXIDATION scores between SMAD4-upregulated and SMAD4-downregulated cells in the CESC1, CESC_ADC, CESC_SCC, and CESC_HSIL groups. *, $p < 0.05$; **, $p < 0.01$; ***, $p < 0.001$. Cervical Squamous Cell Carcinoma and Endocervical Adenocarcinoma, CESC; High-grade Squamous Intraepithelial Lesion, HSIL

3.5 Subclassification of T, NK and B cells

We separated T, NK and B cells and performed dimensionality reduction cluster analysis separately. A total of 14 cell clusters were obtained, and a bar chart was used to represent the proportion of cell sources in each cluster (Fig. 6A). We then calculated the differentially expressed genes of each subgroup, which were shown using volcano maps (Fig. 6B). Marker genes of each cell subtype were used to show their expression through tSNE diagram, further confirming the correctness of the cell subtype (Fig. 6C). The scores of

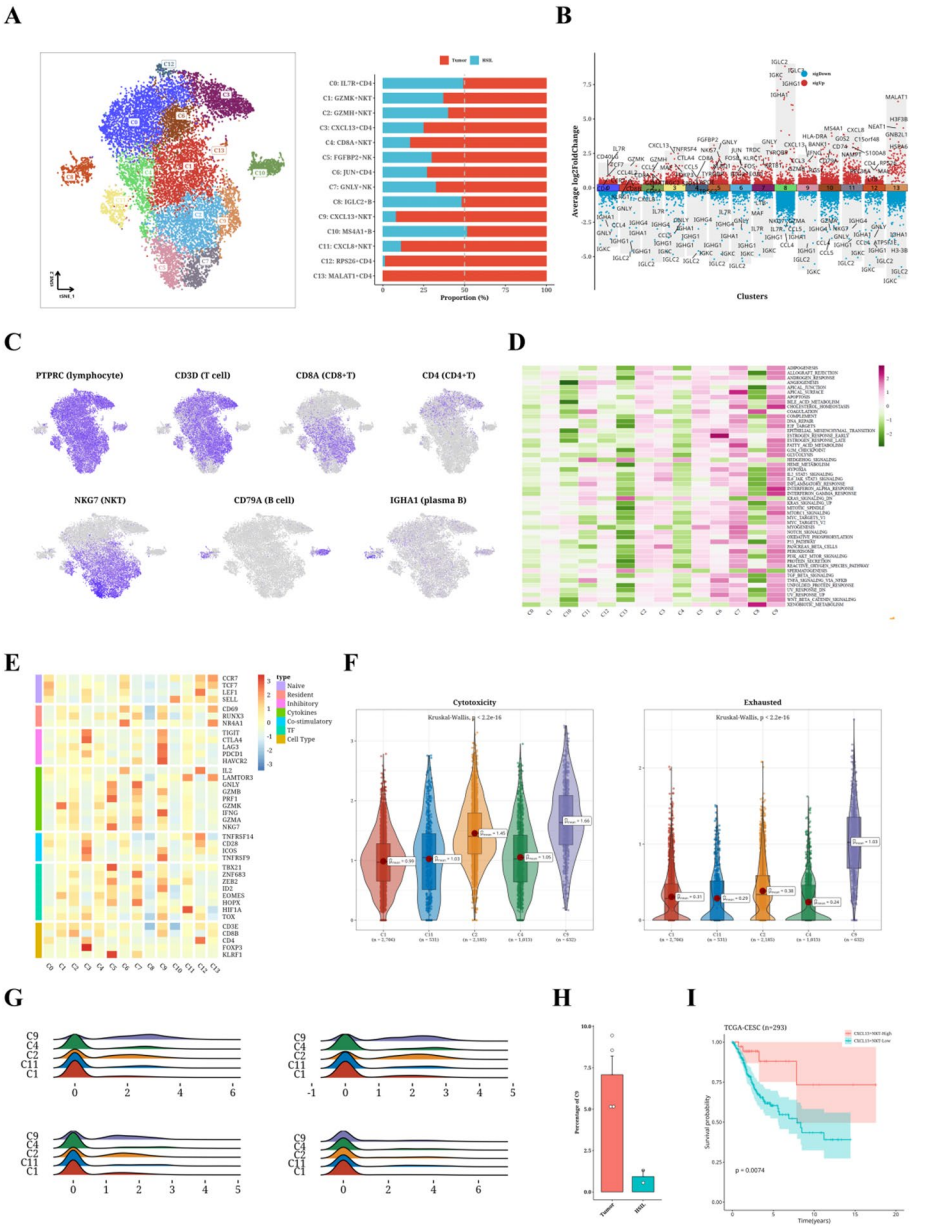

Fig. 6 Subclassification analysis of T, NK cells and B cells, (A) t-SNE diagram of subpopulations of T, NK cells and B cells and cell origin histogram of subpopulations; (B) Differential gene volcano maps for each group; (C) t-Distributed Stochastic Neighbor Embedding (tSNE) diagram of immune cell maker expression; (D) Hallmark heatmap of the scores of the gene sets in each cluster; (E) Heatmap of the expression of immune-related genes in each cluster; (F) Difference in Cytotoxicity and Exhausted values of various subsets of CD8 + cells; (G) Expression ridge map of 4 immune-related genes (GZMB, GZMH, PRF1, GNLY) in CD8 + cell subsets; (H) Histogram of proportion of C9 subgroup in Tumor and HSIL; (I) Kaplan-Meier survival curves show the overall survival probability for patients with a high proportion of CXCL13 + NKT and those with a low proportion of CXCL13 + NKT

Hallmark gene sets in each cluster were calculated and heat maps were drawn (Fig. 6D). The expression of immune genes in each subgroup was shown by heat maps (Fig. 6E). Cytotoxicity and Exhausted values of CD8 + cells were calculated and significant differences were found between CD8 + cell subsets (Fig. 6F). Then, the expression distribution of 4 immune-related genes (GZMB, GZMH, PRF1, GNLY) in CD8 + cell subsets was shown (Fig. 6G). The proportion of C0 subgroup in Tumor and HSIL were compared, and the content of Tumor was significantly higher than that of HSIL (Fig. 6H). Kaplan-Meier survival curves show the overall survival probability for patients with a high proportion of CXCL13 + NKT and those with a low proportion of CXCL13 + NKT. Survival outcomes for patients with a low proportion of CXCL13 + NKT were significantly worse than those with a high proportion of CXCL13 + NKT (log-rank test, $p = 0.0074$). (Fig. 6I).

3.6 Analysis of myeloid cell subpopulations

We isolated myeloid cells for separate dimensionality reduction and clustering analysis, obtaining 12 distinct cell subgroups and displaying their cellular origins (Fig. 7A). We visualized the composition of subgroups in Tumor and HSIL using pie charts (Fig. 7A). Using marker genes for each cell subtype, we illustrated their expression profiles on a tSNE plot, further confirming the accuracy of the cell subtyping (Fig. 7B). The scores of Hallmark gene sets in each subgroup were calculated and depicted in a heatmap (Fig. 7C). Subsequently, we calculated the differentially expressed genes for each subgroup and presented them using volcano plots (Fig. 7D). We analyzed the cellular trajectory of macrophages, with HSIL cells as the starting point, revealing a path of cell differentiation (Fig. 7E). Furthermore, we performed heatmap analysis of the expression of immune genes related to macrophage subgroups (Fig. 7F). The scores for M1 and M2 macrophages were calculated and displayed on a tSNE plot (Fig. 7G). Additionally, we conducted violin plots for differences between subgroups, which showed significant differences among them (Fig. 7H).

3.7 Subgroup analysis of stromal cells

We isolated stromal cells to conduct a dimensionality reduction and clustering analysis, identifying 11 distinct cell subpopulations and illustrating their cellular origins (Figs. 8A-B). Marker genes specific to each cell subtype were utilized to depict their expression profiles on tSNE plots, thereby further validating the correctness of the cell subtyping (Fig. 8C). Subsequently, we determined the differentially expressed genes across the various subgroups and presented them using differential expression heatmaps, with myoCAF, iCAF, and endothelial cells each forming distinct clusters (Fig. 8D). The scores of Hallmark gene sets within each subgroup were calculated and displayed in a heatmap (Fig. 8E). Thereafter, the content of fibroblasts and endothelial localized cellular composition in each empty vector sample was shown, revealing a higher content of fibroblasts compared to a lower content of endothelial cells (Fig. 8F-G).

3.8 Cell communication analysis

We conducted cell communication analyses for both Tumor and HSIL cells, comparing the results and generating network diagrams (Fig. 9A) and scatter plots of communication (Fig. 9B). We selected the MK and GALECTIN signaling pathways for differential comparison using chord diagrams and produced statistical bar charts of ligands (9 C-D).

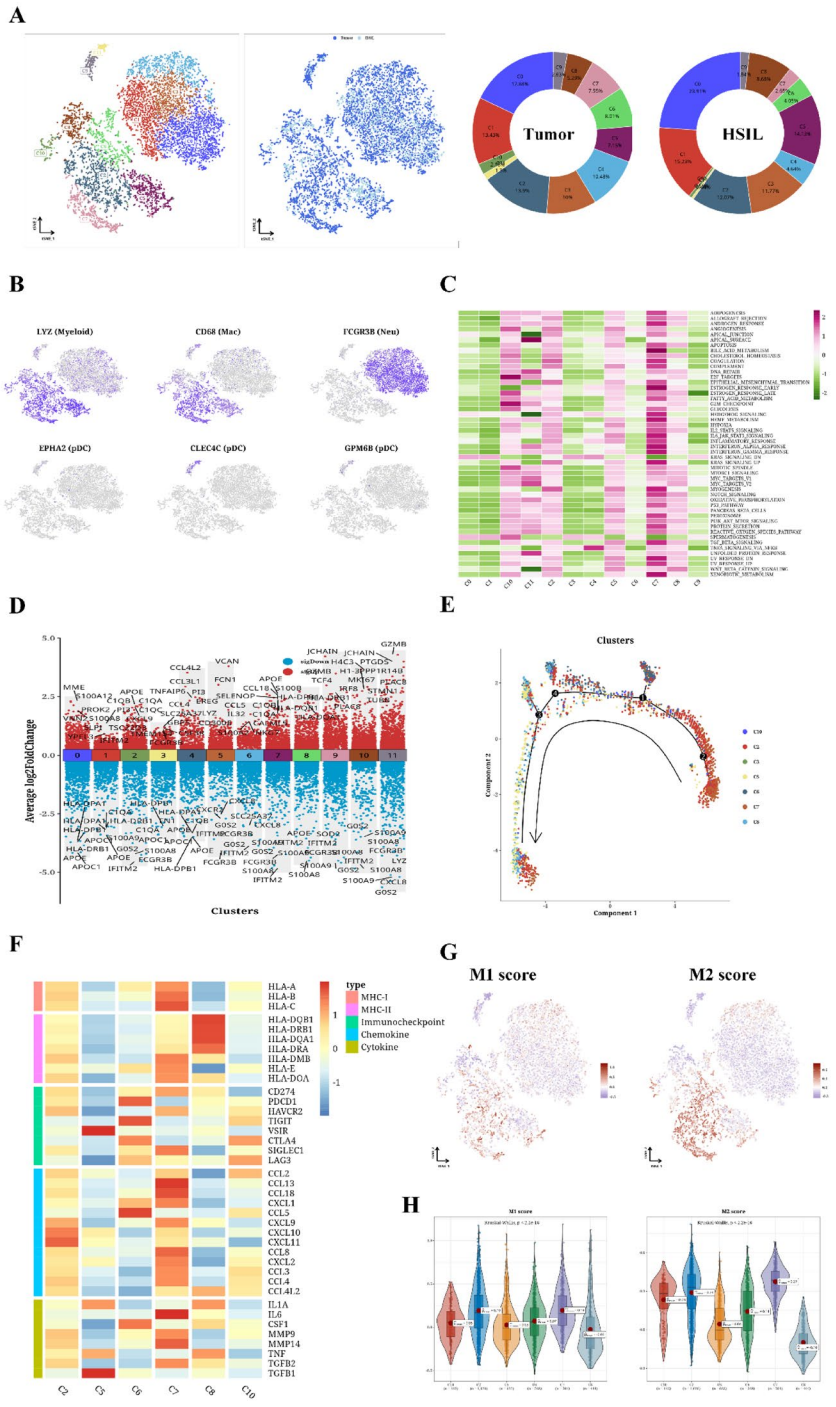

Fig. 7 Analysis results of myeloid cell subsets, (A) Subsets of myeloid cells, cell-derived t-Distributed Stochastic Neighbor Embedding (tSNE) diagram; (B) tSNE diagram of maker expression in subpopulation cells; (C) Hallmark heatmap of the scores of gene sets in each cluster; (D) Differential gene volcano maps for each group; (E) Diagram of cell trajectory analysis of macrophages; (F) Heatmap of the expression of immune-related genes in each cluster; (G) tSNE chart of M1 score and M2 score; (H) The differences of M1 score and M2 score in macrophage subsets violin diagram

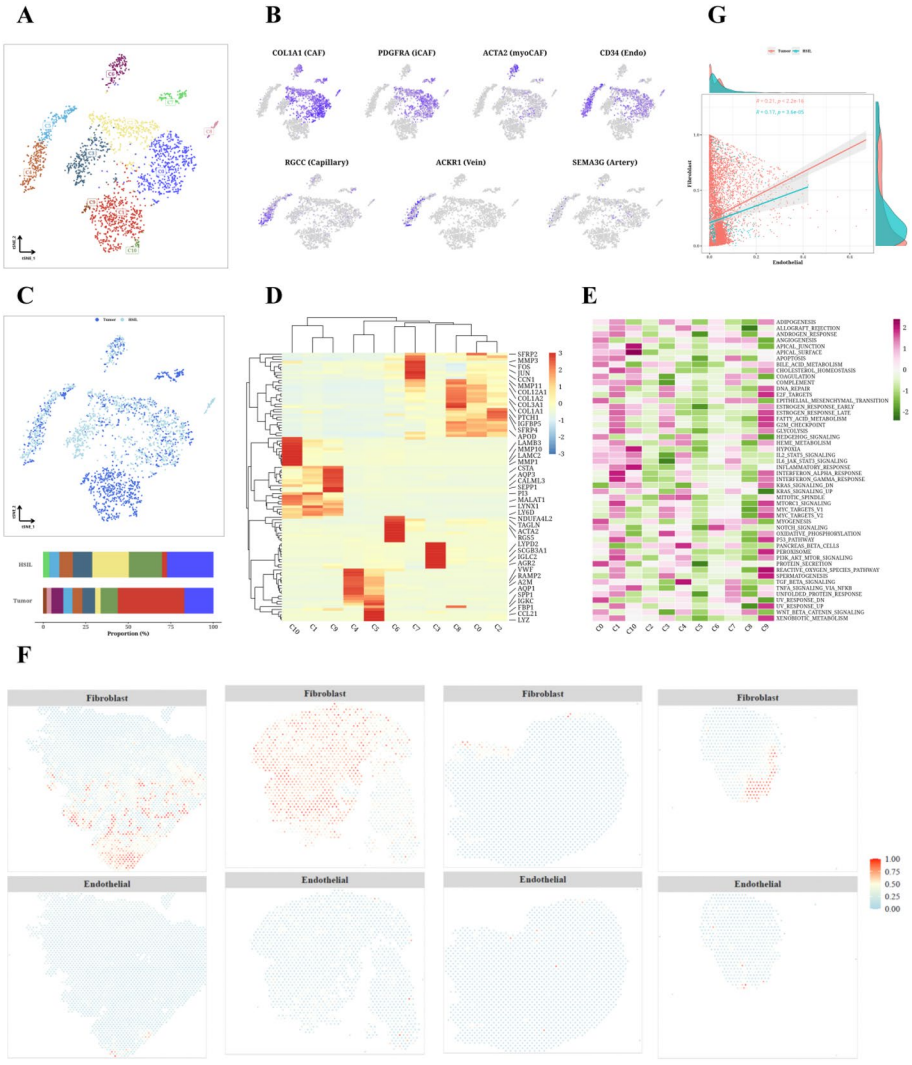

Fig. 8 Subpopulation analysis of stromal cells, (A) t-Distributed Stochastic Neighbor Embedding (t-SNE) diagram of subpopulations of stromal cells; (B) tSNE diagram of maker expression in subpopulation cells; (C) tSNE diagram and bar diagram of cell origin of stromal cells; (D) Expression heat maps of differentially expressed genes in each subgroup; (E) Hallmark heat map of the scores of gene sets in each cluster; F-G. Spatial plots of fibroblasts and endothelial cells in each idling sample

We calculated the expression differences of LGALS9_CD44 and LGALS9_HAVCR2 in the control data (Fig. 9E), revealing that the expression level of LGALS9_CD44 was higher than that of LGALS9_HAVCR2. The findings underscore the nuanced intercellular communication dynamics, illustrating the pivotal roles of specific signaling pathways and receptor-ligand interactions in the cellular milieu of Tumor and HSIL contexts.

4 Discussion

In this study, through spatial transcriptomics and single-cell sequencing technologies, we comprehensively analyzed the tumor microenvironment and dissected tumor heterogeneity in cervical cancer. Utilizing single-cell sequencing, we defined eight cell types within cervical cancer: epithelial cells, fibroblasts, endothelial cells, T cells, NK cells, B cells, myeloid cells, and mast cells. We observed that the proportions of these eight cell types vary among tumors, high-grade squamous intraepithelial lesions, and across

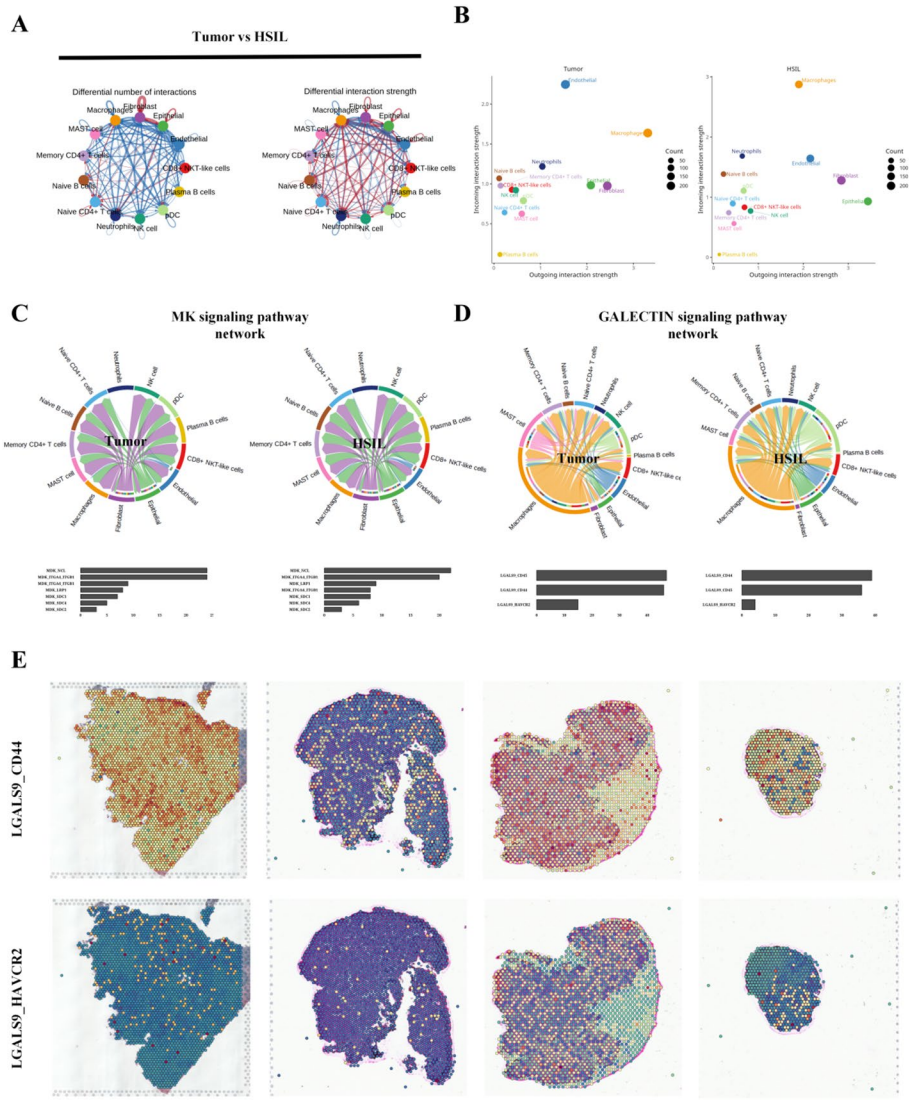

Fig. 9 Cell communication analysis results, A-B. Cell communication network diagram and scatter diagram of two groups of cells; C-D. The chord diagram of the MK and GALECTIN signaling pathways; E. Spatial representation of LGALS9_CD44 and LGALS9_HAVCR2 in idling data. High-grade Squamous Intraepithelial Lesion, HSIL

different tumor samples, indicating dynamic cellular changes and intra-tumor heterogeneity as cervical cancer progresses. Spatial transcriptomics classified stromal cells in adenocarcinoma and squamous cell carcinoma of the cervix, as well as high-grade squamous intraepithelial lesions, into 13 types. By isolating tumor cells for dimensionality reduction and clustering analysis, we identified seven subgroups of tumor/epithelial cells. From the bar charts, we can see the cellular composition of each sample, with Tumor samples containing lots of PI3 + NEO and HSIL samples rich in SLC40A1 + NEO cells. The primary biological function of SLC40A1 is to mediate the export of Fe2 + from key cells involved in iron metabolism (macrophages, intestinal cells, hepatocytes) to the extracellular environment [19].

Numerous studies have identified that SLC40A1, hepcidin (HAMP), and transferrin (TF) play key roles in iron metabolism, with SLC40A1 potentially influencing the progression of high-grade tumorous lesions through ferroptosis [20]. The PI3 gene encodes

a serine protease inhibitor that acts as an antimicrobial peptide against Gram-positive and Gram-negative bacteria, as well as fungal pathogens [21]. This protein contains a WAP-type four-disulfide core (WFDC) domain, making it a member of the WFDC domain family. Most members of the WFDC gene family are located on chromosome 20q12-q13, divided into centromeric and telomeric clusters. This gene belongs to the centromeric gene cluster. The core function of PI3 is to exert antimicrobial, anti-inflammatory, and wound-healing effects by specifically inhibiting the activity of human neutrophil elastase and proteinase-3 [22, 23]. Furthermore, existing studies suggest that PI3 expression may be regulated through interactions with the nuclear factor κB (NF-κB) signaling pathway [24]. This protein regulates the cell cycle by protecting cyclin E from elastase-mediated degradation [25, 26]. More notably, after secretion into the extracellular matrix, PI3 interacts with the epidermal growth factor receptor (EGFR) [27], suggesting its potential to influence the tumor microenvironment via a paracrine mechanism. Although no systematic reports have evaluated the role of PI3 in cervical cancer, research in ovarian cancer has revealed a close association with chemotherapy resistance [28]. Multiple preclinical and clinical studies have demonstrated significantly elevated PI3 expression levels in drug-resistant ovarian cancer tissues. Using gene editing technology, Wei's team showed that modulating PI3 expression directly affects the sensitivity of ovarian cancer cells to cisplatin (CDDP) [28], knockdown enhances chemotherapy sensitivity, while forced expression induces drug resistance. These findings offer critical insights into the mechanism of PI3 in tumor resistance.

Further analysis revealed that FATTY_ACID_BETA_OXIDATION is enriched in PI3 + NEO, and by using the expression level of SMAD4 as a criterion for cell grouping, and calculating the mean for grouping, violin plots indicated significant differences in FATTY_ACID_BETA_OXIDATION scores between the two cell groups. While there is no direct evidence of interaction between PI3 and SMAD4 in the context of fatty acid oxidation, they may be linked through metabolic signaling integration. SMAD4, as a core molecule in the TGF-β pathway, can directly regulate glycolysis, mitochondrial function, and lipid metabolism-related genes, affecting fatty acid oxidation efficiency. PI3 stabilizes the metabolic microenvironment by inhibiting inflammatory factors, potentially indirectly affecting TGF-β signaling activity. SMAD4 deficiency promotes lipid synthesis, while low PI3 expression exacerbates inflammation, jointly disrupting metabolic homeostasis. In cervical cancer, the expression and function of SMAD4 may be influenced by HPV viral proteins, thereby affecting processes such as cell proliferation, differentiation, and apoptosis [29]. TGFBR2 regulates the Hedgehog pathway by mediating SMAD4, influencing cervical cancer cell proliferation and migration [30].Studies show that mutations or dysregulation in SMAD4 are associated with the development of cervical cancer, suggesting SMAD4 as a potential biomarker and therapeutic target for cervical cancer [29].

In our analysis of NKT cells, we identified a group of CXCL13 + NKT cells associated with prognosis. Previous literature reports that levels of CXCL13 are closely related to the clinical prognosis after radical surgery for cervical cancer, and DNA methylation-dependent downregulation of CXCL13 can promote the carcinogenesis and progression of cervical cancer, making it an important predictor of clinical prognosis and strongly suggesting its application in clinical practice [31, 32]. However, more mechanistic studies are still needed. Through subgroup analysis of stromal cells, we found that tumors

have a higher content of fibroblasts and a lower content of endothelial cells. Studies on fibroblasts in cervical cancer have been focusing on their role in tumor microenvironment modulation, contribution to cancer progression, and resistance to therapy. Researchers are particularly interested in how cancer-associated fibroblasts (CAFs) support tumor growth, influence immune cell infiltration, and could be targeted for therapeutic purposes. In our final analysis of Tumor and HSIL cells, cell communication revealed upregulation of the MK and GALECTIN signaling pathways in tumors. The role of the GALECTIN family proteins in tumorigenesis and development has become a focal point of research, including their functions in cell adhesion, proliferation, apoptosis, and immune evasion. In cervical cancer, GALECTINS may play a role by modulating the tumor microenvironment and affecting the interactions between tumor cells and immune cells.

Single-cell sequencing and spatial transcriptomics studies have shown that LGALS9 expression in CESC tumors is significantly higher than in non-cancerous samples [33]. High LGALS9 expression binds to the TIM-3 receptor on the surface of T cells, inhibiting the secretion of cytokines (such as IFN-γ and TNF-α) by CD8 + T cells, reducing T cell proliferation and suppressing CD8 + T cell function [34, 35]. LGALS9 also binds to PD-1, inhibiting T cell apoptosis. Studies in head and neck squamous cell carcinoma have demonstrated that HPV-encoded circular RNA significantly enhances CD8 + T cell activity by downregulating LGALS9 expression, thereby improving patient survival [36]. High LGALS9 expression contributes to a highly immunosuppressive tumor microenvironment, which may be associated with chemotherapy resistance, ineffective immunotherapy, and poor prognosis. PD-1 is a ligand for LGALS9, and its binding inhibits T cell apoptosis [37]. However, overexpression of LGALS9 may negate PD-1 expression in the tumor microenvironment. In clinical treatment, the response rate to monotherapy with PD-1/PD-L1 inhibitors in cervical cancer is low. However, PD-1/TIM-3 bispecific antibodies, which can simultaneously block two immunosuppressive pathways, have demonstrated potential superiority over monotherapy in clinical trials. Therefore, LGALS9 may become a biomarker for predicting response to immunotherapy, providing a new direction for personalized treatment of cervical cancer.

This study has several limitations. First, it relied solely on publicly available sequencing data and lacked further validation through in vivo and in vitro experiments. This lack of experimental validation may have influenced the results, which makes it difficult to definitively confirm the biological functions and significance of the key molecules identified in actual physiological or pathological settings. Second, further exploration of the mechanisms underlying these key molecules is needed. To address this validation issue, future studies could employ potential experimental approaches. Functional assays, including gene knockdown or overexpression experiments in cell lines, can be used to assess the direct effects of key molecules on cervical cancer related cellular processes, such as cell proliferation, migration, and invasion. Patient derived organoids can serve as more physiologically relevant models and, by reducing the use of experimental animals, comply with animal ethics requirements. These organoids can, to a certain extent, mimic the in vivo tumor microenvironment, allowing for a better understanding of how the identified molecules interact with other cell types and factors in the context of cervical cancer. Combining these approaches will provide a more balanced perspective and guide future research directions.

Acknowledgements
Not applicable.

Author contributions
Yinxia Yang designed the study pipeline and wrote the manuscript. Yinxia Yang and Bohui Zhou performed date collection and sorting. Yinxia Yang, Sirong Cheng, Yuxuan Zhong, Pengyu Sun and Xiaoru Deng obtained all the pictures. Finally, Bohui Zhou reviewed and revised the manuscript in detail.

Funding
This study was supported by Fundamental Research Program of Shanxi Province (Grant No. 202203021212101).

Data availability
The datasets analyzed during the current study are available in the TCGA (https://portal.gdc.cancer.gov/) and GEO (https://www.ncbi.nlm.nih.gov/geo/) repository.

Declarations

Ethics approval and consent to participate
This study used only previously published single-cell transcriptome and spatial transcriptome data from cervical cancer and cervical intraepithelial lesions, for which appropriate ethical approval and participant consent were obtained. As a secondary analysis of existing sequencing data, this study did not require additional ethical approval.

Consent for publication
Not applicable.

Competing interests
The authors declare no competing interests.

Received: 6 August 2025 / Accepted: 6 November 2025
Published online: 27 November 2025

References

1. Adam MA, Pura J, Goffredo P, Dinan MA, Reed SD, Scheri RP, Hyslop T, Roman SA, Sosa JA. Presence and Number of Lymph Node Metastases Are Associated With Compromised Survival for Patients Younger Than Age 45 Years With Papillary Thyroid Cancer. *J Clin Oncol*. Jul 20. 2015;33(21):2370-5. https://doi.org/10.1200/JCO.2014.59.8391.
2. Singh D, Vignat J, Lorenzoni V, Eslahi M, Ginsburg O, Lauby-Secretan B, Arbyn M, Basu P, Bray F, Vaccarella S. Feb. Global estimates of incidence and mortality of cervical cancer in 2020: a baseline analysis of the WHO Global Cervical Cancer Elimination Initiative. *Lancet Glob Health*. 2023;11(2):e197-e206. https://doi.org/10.1016/s2214-109x(22)00501-0.
3. Qiu H, Cao S, Xu R. Oct. Cancer incidence, mortality, and burden in China: a time-trend analysis and comparison with the United States and United Kingdom based on the global epidemiological data released in 2020. *Cancer Commun (Lond)*. 2021;41(10):1037–1048. https://doi.org/10.1002/cac2.12197.
4. Walboomers JM, Jacobs MV, Manos MM, Bosch FX, Kummer JA, Shah KV, Snijders PJ, Peto J, Meijer CJ, Muñoz N. Sep. Human papillomavirus is a necessary cause of invasive cervical cancer worldwide. *J Pathol*. 1999;189(1):12 – 9. https://doi.org/10.1002/%28SICI%291096-9896%28199909%29189:1%3C12::AID-PATH431%3E3.0.CO;2-F.
5. Fujiwara H, Yokota H, Monk B, Treilleux I, Devouassoux-Shisheboran M, Davis A, Kim JW, Mahner S, Stany M, Pignata S, Ray-Coquard I, Fujiwara K. Nov. Gynecologic Cancer InterGroup (GCIG) consensus review for cervical adenocarcinoma. *Int J Gynecol Cancer*. 2014;24(9 Suppl 3):S96-101. https://doi.org/10.1097/igc.0000000000000263.
6. Shalaby NA, Tudorescu-Morjan C, Manole CG, Iacata AA, Popovici ML, Grecu LI, Curici A. Mar. Correlation between high-risk HPV infection and p16/Ki-67 abnormalities in Pap samples in a South Eastern Europe cohort. *J Med Virol*. 2024;96(3):e29524. https://doi.org/10.1002/jmv.29524.
7. Moody C. Mechanisms by which HPV Induces a Replication Competent Environment in Differentiating Keratinocytes. *Viruses*. Sep 19. 2017;9(9). https://doi.org/10.3390/v9090261.
8. Mirabello L, Yeager M, Cullen M, Boland JF, Chen Z, Wentzensen N, Zhang X, Yu K, Yang Q, Mitchell J, Roberson D, Bass S, Xiao Y, Burdett L, Raine-Bennett T, Lorey T, Castle PE, Burk RD, Schiffman M. Sep. HPV16 Sublineage Associations With Histology-Specific Cancer Risk Using HPV Whole-Genome Sequences in 3200 Women. *J Natl Cancer Inst*. 2016;108(9). https://doi.org/10.1093/jnci/djw100.
9. Mazurec K, Trzeszcz M, Mazurec M, Streb J, Halon A, Jach R. Mar. Should we use risk selection tests for HPV 16 and/or 18 positive cases: Comparison of p16/Ki67 and cytology. *J Med Virol*. 2024;96(3):e29500. https://doi.org/10.1002/jmv.29500.
10. Su DG, Schoenfeld DA, Ibrahim W, Cabrejo R, Djureinovic D, Baumann R, Rimm DL, Khan SA, Halaban R, Kluger HM, Olino K, Galan A, Clune J. Digital spatial proteomic profiling reveals immune checkpoints as biomarkers in lymphoid aggregates and tumor microenvironment of desmoplastic melanoma. *J Immunother Cancer*. Mar 21. 2024;12(3). https://doi.org/10.1136/jitc-2023-008646.
11. Silva TC, Colaprico A, Olsen C, D'Angelo F, Bontempi G, Ceccarelli M, Noushmehr H. TCGA Workflow: Analyze cancer genomics and epigenomics data using Bioconductor packages. *F1000Research*. 2016;5:1542. https://doi.org/10.12688/f1000research.8923.2.
12. Hao Y, Hao S, Andersen-Nissen E, Mauck WM 3rd, Zheng S, Butler A, Lee MJ, Wilk AJ, Darby C, Zager M, Hoffman P, Stoeckius M, Papalexi E, Mimitou EP, Jain J, Srivastava A, Stuart T, Fleming LM, Yeung B, Rogers AJ, McElrath JM, Blish CA, Gottardo R, Smibert P, Satija R. Integrated analysis of multimodal single-cell data. *Cell*. Jun 24. 2021;184(13):3573–3587.e29. https://doi.org/10.1016/j.cell.2021.04.048.

13. Korsunsky I, Millard N, Fan J, Slowikowski K, Zhang F, Wei K, Baglaenko Y, Brenner M, Loh PR, Raychaudhuri S. Fast, sensitive and accurate integration of single-cell data with Harmony. *Nature methods*. 2019/12/01 2019;16(12):1289–1296. https://doi.org/10.1038/s41592-019-0619-0.
14. Hafemeister C, Satija R. Normalization and variance stabilization of single-cell RNA-seq data using regularized negative binomial regression. *Genome biology*. Dec 23. 2019;20(1):296. https://doi.org/10.1186/s13059-019-1874-1.
15. Ma Y, Zhou X. Spatially informed cell-type deconvolution for spatial transcriptomics. *Nature biotechnology*. 2022/09/01 2022;40(9):1349–1359. https://doi.org/10.1038/s41587-022-01273-7.
16. Hänzelmann S, Castelo R, Guinney J. GSVA: gene set variation analysis for microarray and RNA-seq data. *BMC bioinformatics*. Jan 16. 2013;14:7. https://doi.org/10.1186/1471-2105-14-7.
17. Trapnell C, Cacchiarelli D, Grimsby J, Pokharel P, Li S, Morse M, Lennon NJ, Livak KJ, Mikkelsen TS, Rinn JL. Apr. The dynamics and regulators of cell fate decisions are revealed by pseudotemporal ordering of single cells. *Nature biotechnology*. 2014;32(4):381–386. https://doi.org/10.1038/nbt.2859.
18. Jin S, Guerrero-Juarez CF, Zhang L, Chang I, Ramos R, Kuan CH, Myung P, Plikus MV, Nie Q. Inference and analysis of cell-cell communication using CellChat. *Nature communications*. 2021/02/17 2021;12(1):1088. https://doi.org/10.1038/s41467-021-21246-9.
19. Donovan A, Lima CA, Pinkus JL, Pinkus GS, Zon LI, Robine S, Andrews NC. Mar. The iron exporter ferroportin/Slc40a1 is essential for iron homeostasis. *Cell metabolism*. 2005;1(3):191–200. https://doi.org/10.1016/j.cmet.2005.01.003.
20. Erslev AJ, Soltan A. Pure redMar -cell aplasia: a review. *Blood Rev*. 1996;10(1):20 – 8. https://doi.org/10.1016/s0268-960x(96)90017-x.
21. Longatto-Filho A, Fregnani JH, Mafra da Costa A, de Araujo-Souza PS, Scapulatempo-Neto C, Herbster S, Boccardo E, Termini L. Evaluation of Elafin Immunohistochemical Expression as Marker of Cervical Cancer Severity. *Acta Cytol*. 2021;65(2):165–174. https://doi.org/10.1159/000512010.
22. Verrier T, Solhonne B, Sallenave JM, Garcia-Verdugo I. The WAP protein Trappin-2/Elafin: a handyman in the regulation of inflammatory and immune responses. Int J Biochem Cell Biol. 2012;44(8):1377–80. https://doi.org/10.1016/j.biocel.2012.05.007.
23. Williams SE, Brown TI, Roghanian A, Sallenave JM. SLPI and elafin: one glove, many fingers. Clin Sci (Lond). 2006;110(1):21–35. https://doi.org/10.1042/CS20050115.
24. Clauss A, Ng V, Liu J, Piao H, Russo M, Vena N, Sheng Q, Hirsch MS, Bonome T, Matulonis U, Ligon AH, Birrer MJ, Drapkin R. Overexpression of Elafin in ovarian carcinoma is driven by genomic gains and activation of the nuclear factor kappab pathway and is associated with poor overall survival. Neoplasia. 2010;12(2):161–72. https://doi.org/10.1593/neo.91542.
25. Bouchard D, Morisset D, Bourbonnais Y, Tremblay GM. Proteins with whey-acidic-protein motifs and cancer. Lancet Oncol. 2006;7(2):167–74. https://doi.org/10.1016/S1470-2045(06)70579-4.
26. Labidi-Galy SI, Clauss A, Ng V, Duraisamy S, Elias KM, Piao HY, Bilal E, Davidowitz RA, Lu Y, Badalian-Very G, Györffy B, Kang UB, Ficarro S, Ganesan S, Mills GB, Marto JA, Drapkin R. Elafin drives poor outcome in high-grade serous ovarian cancers and basal-like breast tumors. Oncogene. 2015;34(3):373–83. https://doi.org/10.1038/onc.2013.562.
27. Wang C, Liao Y, He W, Zhang H, Zuo D, Liu W, Yang Z, Qiu J, Yuan Y, Li K, Zhang Y, Wang Y, Shi Y, Qiu Y, Gao S, Yuan Y, Li B. Elafin promotes tumour metastasis and attenuates the anti-metastatic effects of erlotinib via binding to EGFR in hepatocellular carcinoma. J Exp Clin Cancer Res. 2021;40(1):113. https://doi.org/10.1186/s13046-021-01904-y.
28. Wei H, Hellström KE, Hellström I. Elafin selectively regulates the sensitivity of ovarian cancer cells to genotoxic drug-induced apoptosis. Gynecol Oncol. 2012;125(3):727–33. https://doi.org/10.1016/j.ygyno.2012.03.018.
29. Citro S, Miccolo C, Medda A, Ghiani L, Tagliabue M, Ansarin M, Chiocca S. HPV-mediated regulation of SMAD4 modulates the DNA damage response in head and neck cancer. *Journal of experimental & clinical cancer research: CR*. Feb 10. 2022;41(1):59. https://doi.org/10.1186/s13046-022-02258-9.
30. Yuan J, Yi K, Yang L. TGFBR2 Regulates Hedgehog Pathway and Cervical Cancer Cell Proliferation and Migration by Mediating SMAD4. *J Proteome Res*. Aug 7. 2020;19(8):3377–3385. https://doi.org/10.1021/acs.jproteome.0c00239.
31. Hu XX, Zhou LY, Lin RY. Dec. The association between the serum concentration of CXC subfamily chemokine 13 and post-surgical clinical outcomes in cervical cancer patients. *Eur Rev Med Pharmacol Sci*. 2023;27(23):11635–11642. https://doi.org/10.26355/eurrev_202312_34601.
32. Ma D, Fan SB, Hua N, Li GH, Chang Q, Liu X. Hypermethylation of Single CpG Dinucleotides at the Promoter of CXCL13 Gene Promoting Cell Migration in Cervical Cancer. *Curr Cancer Drug Targets*. 2020;20(5):355–363. https://doi.org/10.2174/1568009620666200102123635.
33. Mendieta-Carmona V, Delgado-López G, Reyes-Leyva J, Gutiérrez-Quiroz CT, Vazquez-Zamora VJ, Picazo-Mendoza DA, Montiel-Jarquín AJ, Martinez-Morales LP, Vallejo-Ruiz V. Galectin-9 Expression is Correlated to Cervical Squamous Cell Carcinoma Progression and Overall Survival. *OncoTargets and therapy*. 2023;16:891–904. https://doi.org/10.2147/ott.S433710.
34. Llaó-Cid L, Wong J, Fernandez Botana I, Paul Y, Wierz M, Pilger LM, Floerchinger A, Tan CL, Gonder S, Pagano G, Chazotte M, Bestak K, Schifflers C, Iskar M, Roider T, Czernilofsky F, Bruch PM, Mallm JP, Cosma A, Campton DE, Gerhard-Hartmann E, Rosenwald A, Colomer D, Campo E, Schapiro D, Green EW, Dietrich S, Lichter P, Moussay E, Paggetti J, Zapatka M, Seiffert M. Integrative multi-omics reveals a regulatory and exhausted T-cell landscape in CLL and identifies galectin-9 as an immunotherapy target. Nat Commun. 2025;16(1):7271. https://doi.org/10.1038/s41467-025-61822-x.
35. Lv Y, Ma X, Ma Y, Du Y, Feng J. A new emerging target in cancer immunotherapy: Galectin-9 (LGALS9). Genes Dis. 2022;10(6):2366–82. https://doi.org/10.1016/j.gendis.2022.05.020.
36. Ge J, Meng Y, Guo J, Chen P, Wang J, Shi L, Wang D, Qu H, Wu P, Fan C, Zhang S, Liao Q, Zhou M, Xiang B, Wang F, Tan M, Gong Z, Xiong W, Zeng Z. Human papillomavirus-encoded circular RNA circE7 promotes immune evasion in head and neck squamous cell carcinoma. Nat Commun. 2024;15(1):8609. https://doi.org/10.1038/s41467-024-52981-4.
37. Yang R, Sun L, Li CF, Wang YH, Yao J, Li H, Yan M, Chang WC, Hsu JM, Cha JH, Hsu JL, Chou CW, Sun X, Deng Y, Chou CK, Yu D, Hung MC. Galectin-9 interacts with PD-1 and TIM-3 to regulate T cell death and is a target for cancer immunotherapy. Nat Commun. 2021;12(1):832. https://doi.org/10.1038/s41467-021-21099-2.

Publisher's note